Simulink Model for PWM-Supplied Laminated Magnetic Cores Including Hysteresis, Eddy-Current, and Excess Losses

Paavo Rasilo, *Member, IEEE*, Wilmar Martinez, *Member, IEEE*, Keisuke Fujisaki, *Senior Member, IEEE*, Jorma Kyyrä, *Member, IEEE*, and Alex Ruderman, *Senior Member, IEEE*

***Abstract*—A new implementation of an iron-loss model for laminated magnetic cores in the MATLAB/Simulink environment is proposed in this paper. The model is based on numerically solving a one-dimensional diffusion problem for the eddy currents in the core lamination and applying an accurate hysteresis model as the constitutive law. An excess loss model is also considered. The model is identified merely based on the catalog data provided by the core material manufacturer. The implementation is validated with analytical and finite-element models and experimentally in the case of a toroidal inductor supplied from a GaN FET full-bridge inverter with 5–500 kHz switching frequencies and a deadtime of 300 ns. Despite the simple identification, a good correspondence is observed between the simulated and measured iron losses, the average difference being 3.3% over the wide switching frequency range. It is shown that accounting for the skin effect in the laminations is significant, in order to correctly model the iron losses at different switching frequencies. Some differences between the measured and simulated results at high switching frequencies are also discussed. The model is concluded to be applicable for designing and analyzing laminated magnetic cores in combination with power-electronics circuits. The Simulink models are openly available.**

***Index Terms*—Eddy currents, hysteresis, inductors, inverters, pulsewidth modulation.**

Manuscript received January 24, 2018; revised March 19, 2018; accepted May 3, 2018. Date of publication June 4, 2018; date of current version December 7, 2018. This work was supported in part by the Academy of Finland and in part by the Emil Aaltonen Foundation. Recommended for publication by Associate Editor B. Chen. *(Corresponding author: Paavo Rasilo.)*

P. Rasilo is with the Laboratory of Electrical Energy Engineering, Tampere University of Technology, Tampere 33101, Finland, and also with the Department of Electrical Engineering and Automation, Aalto University, Aalto 00076, Finland (e-mail: paavo.rasilo@tut.fi).

W. Martinez was with the Department of Electrical Engineering and Automation, Aalto University, Aalto 00076, Finland. He is now with the Department of Electrical Engineering (ESAT), KU Leuven, Diepenbeek 3590, Belgium (e-mail: wilmar.martinez@kuleuven.be).

K. Fujisaki is with the Toyota Technological Institute, Tenpaku 468-8511, Japan (e-mail: fujisaki@toyota-ti.ac.jp).

J. Kyyrä is with the Department of Electrical Engineering and Automation, Aalto University, Aalto 00076, Finland (e-mail: jorma.kyyra@aalto.fi).

A. Ruderman is with the Power Electronics Research Lab, School of Engineering, Nazarbayev University, Astana 010000, Kazakhstan (e-mail: alexander.ruderman@nu.edu.kz).

Color versions of one or more of the figures in this paper are available online at http://ieeexplore.ieee.org.

Digital Object Identifier 10.1109/TPEL.2018.2835661

I. Introduction

MAGNETIC components used in power-electronics applications are subject to complex flux-density waveforms with high-frequency components, which give rise to power losses. Novel low-loss materials such as nanocrystalline [1] and amorphous alloys [2], and soft magnetic composites [3] have been developed to keep the losses in reasonable limits despite the rapidly increasing switching frequencies [4], [5]. However, thin steel laminations still provide the most cost-efficient solution for transformer cores [6], [7] and are also commonly used in electrical machines [8], [9] supplied by power converters. Accurate core-loss models are needed for electromagnetic and thermal design of magnetic components with high power densities and energy-efficiencies.

Review of literature from the recent years gives the impression that loss calculation methods applied in the analysis and design of magnetic components used in power-electronics applications are still majorly based on frequency-domain Steinmetz- or Bertotti-type formulas [7], [10]–[13]. Identification of such models typically requires a large amount of measurements as well as empirical correction factors in order to tune the parameters to the waveforms and operating conditions under consideration. For example, nonsinusoidal flux-density waveforms are accounted for by estimating an average frequency over a closed excitation cycle [7], [10], and accounting for dc bias would require measurement of additional correction factors [11].

Some frequency-domain models are based on more theoretical considerations, but often with overly simplifying assumptions. For example, in [14], eddy-current losses for each magnetic field strength harmonic were superposed assuming linear magnetization properties. In [15], a frequency-domain equivalent circuit approach was derived from the physical behavior of the electromagnetic field in the core. However, also this model assumes linear magnetic behavior and can only predict small-signal behavior of the eddy-currents.

Time-domain approaches aim to provide general expressions directly applicable with different excitation waveforms, but such models are surprisingly rarely used in the field of power electronics. Time-domain extensions of the Bertotti- and Steinmetz-type eddy-current loss models coupled to hysteresis models were

presented in [16]–[20]. In [21], the Jiles-Atherton-hysteresis model was applied for loss prediction in a ferrite inductor. Pulsewidth modulated (PWM) converter voltage quality and its relation to the core losses were discussed in [22].

Starting from Maxwell equations, eddy-current losses in laminated magnetic cores can be accurately calculated by numerically solving a nonlinear one-dimensional (1-D) diffusion equation for the magnetodynamic field [23]–[27]. If hysteresis losses are also of interest, a hysteresis model needs to be used as a constitutive law, when the 1-D problem is solved. A new history-dependent hysteresis model (HDHM) was described by Zirka *et al*. in [28]. The model is easy to identify and able to describe minor hysteresis loops, which is essential for applications including power-electronic converters. So far the model has been applied in circuit simulation tools for analyzing single- and three-phase transformers mainly in low-frequency applications and with sinusoidal supply voltages [29]–[33]. To our experience, the model of [28] clearly overrides Preisach-type hysteresis models [9] in its simpleness, computation speed, and numerical stability, and thus seems promising for analyzing devices with complex flux-density waveforms. Although [28] proposes coupling the HDHM to a numerical 1-D eddy-current model in core laminations, in the practical applications mainly simplified dynamic eddy-current models tuned for grain-oriented steels and sinusoidal excitations have been used for the simulations [30], [32], [33]. It is not clear if such models are suitable for applications including high-frequency switching harmonics. Numerical 1-D eddy-current models have been coupled to hysteresis models and further to finite-element (FE) solvers [25]–[27], but implementations of such models in circuit simulation tools for analyzing power converters have not yet been reported in details.

In this paper, we combine the 1-D eddy-current loss model of [24] and [25] to the hysteresis model of [28] and a time-domain excess-loss model of [34], and describe how the resulting iron-loss model can be implemented in the MATLAB / Simulink environment. The main advantage of a Simulink implementation is the straightforward coupling to Simscape models, which allow simulating complex physical systems using a block diagram approach. Simscape includes built-in components for switches and converters and thus, the developed model offers a simple tool for considering iron losses in the design and analysis of magnetic cores coupled with switching devices. The developed models can be identified directly from the magnetization curves and material parameters typically given in manufacturer catalogs, making it easier to adopt the models for everyday design purposes.

The developed model is compared to analytical and two-dimensional (2-D) FE models and applied to replicate the measurement conditions described in [35]. A laminated toroidal core supplied from a GaN FET inverter is measured and simulated up to 500 kHz switching frequencies accounting for the 300 ns deadtime used in the measurements. The simulated and measured core losses are shown to match well, although some differences at higher switching frequencies are also pointed out.

TABLE I
SPECIFICATIONS OF THE TOROIDAL TEST INDUCTOR

Core material	Nippon 35H300
Lamination thickness d	0.35 mm
Electrical conductivity σ	1.92 MS/m
Mass density ρ	7650 kg/m^3
Outer diameter	127 mm
Inner diameter	102 mm
Number of laminations in stack	20
Cross-sectional area A_{Fe}	87.5 mm^2
Flux-path length l_{Fe}	360 mm
Number of primary turns N_1	254
Number of secondary turns N_2	254

(a)

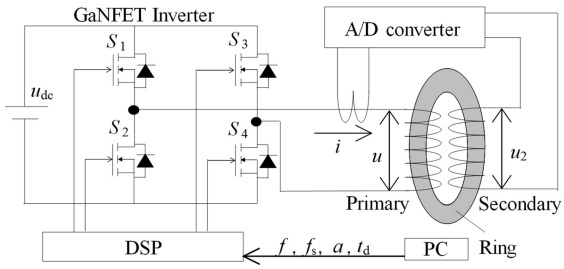

(b)

Fig. 1. (a) Test inductor. (b) Schematic of the measurement setup.

II. MEASUREMENTS

A toroidal laminated-core inductor with primary and secondary windings is used as a test device. The measurement setup is described in detail in [35]. The primary is supplied from a full-bridge inverter with GaN FET switches. Specifications of the test inductor are given in Table I. A picture of the test inductor is shown in Fig. 1(a) and a schematic of the measurement setup is shown in Fig. 1(b).

Magnetic field strength h_{s} on the surface of the iron core is calculated from the measured primary winding current i as follows:

$$h_{\mathrm{s}}(t) = \frac{N_1}{l_{\mathrm{Fe}}} i(t) \tag{1}$$

where N_1 is the number of primary turns and l_{Fe} is the length of the flux path. Average magnetic flux density in the core is obtained by integrating the back-electromotive force u_2 induced

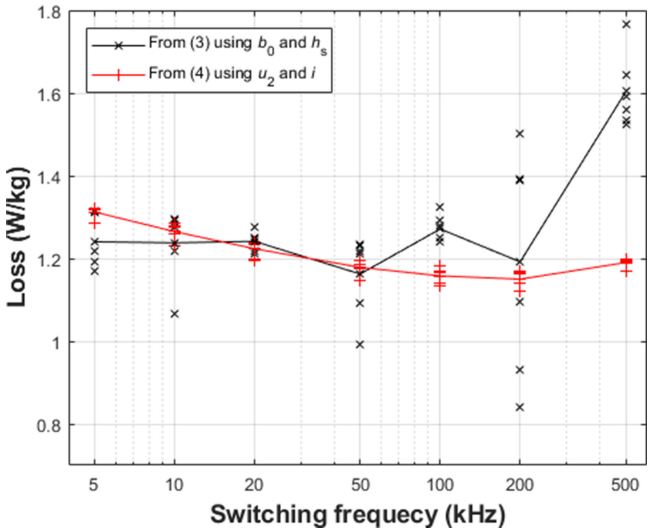

Fig. 2. Losses measured from the test inductor at 5 – 500 kHz switching frequencies. The markers denote the six separate measurements for each switching frequency. The lines are drawn through the average values. Results calculated with (3) and (4) are shown.

into a secondary winding with N_2 turns as follows:

$$b_0(t) = \frac{1}{N_2 A_{\mathrm{Fe}}} \int u_2(t)\, dt \tag{2}$$

where A_{Fe} is the cross-sectional area of the laminated core. The core loss density per unit mass is obtained from the measured dynamic $b_0(h_s)$ loop, during one period of the fundamental frequency f as follows:

$$p_{\mathrm{tot}} = \frac{f}{\rho} \int_0^{1/f} h_s(t) \frac{db_0(t)}{dt} dt \tag{3}$$

or alternatively from

$$p_{\mathrm{tot}} = \frac{N_1 f}{N_2 A_{\mathrm{Fe}} l_{\mathrm{Fe}} \rho} \int_0^{1/f} i(t)\, u_2(t)\, dt \tag{4}$$

where ρ is the mass density.

The core losses in the inductor were measured at a fundamental frequency of $f = 50$ Hz and switching frequencies ranging from $f_s = 5$ to 500 kHz. A modulation index $a = 0.5$ was used, and the dc-link voltage u_{dc} was adjusted so that a magnetic flux-density amplitude of 1 T was obtained. Depending on the switching frequency, the dc-link voltages varied around 15–16 V. For each switching frequency, six separate measurements were taken. Although (3) and (4) are theoretically equivalent, (3) easily suffers from numerical inaccuracies if the integration in (2) and differentiation in (3) are not consistent with each other. Indeed, Fig. 2 shows the variation of the measured core losses calculated using both the equations. It is seen that the variation in the losses calculated with (3) is significantly larger than the variation in the losses calculated with (4). When comparing the simulated and measured results in the latter sections, the losses calculated with (4) are used.

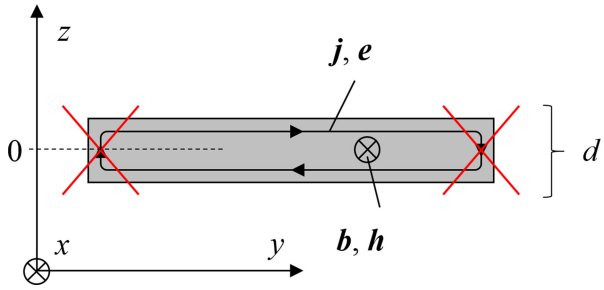

Fig. 3. Problem setting for the 1-D eddy-current problem.

III. Models for the Laminated Core

A. Eddy-Current Loss Model

A model for describing eddy-current losses in a core lamination, with a thickness d and electrical conductivity σ, has been developed in [24] and [25]. We describe the model in a rather detailed manner in order to back up the Simulink implementation in the upcoming sections. For the considered nonoriented grade 35H300, the material parameters obtained from the manufacturer catalog [36] are presented in Table I.

The plane of the lamination is assumed to lie in the xy plane, such that the thickness is placed along the z-direction: $z \in [-d/2, d/2]$, see Fig. 3. Since only single-phase devices without rotational magnetic fields are considered, the magnetic flux density $\boldsymbol{b}(z,t) = b(z,t)\boldsymbol{u}_x$ and field strength $\boldsymbol{h}(z,t) = h(z,t)\boldsymbol{u}_x$ are assumed to be fixed to the x-direction and to depend only on the position z along the thickness. The Gauss law $\nabla \cdot \boldsymbol{b} = 0$ is automatically satisfied, and the electromagnetic field is described by the Faraday's law and the (quasi-static) Ampere's law as follows:

$$\nabla \times \boldsymbol{e}(z,t) = -\frac{\partial \boldsymbol{b}(z,t)}{\partial t} \tag{5}$$

$$\nabla \times \boldsymbol{h}(z,t) = \boldsymbol{j}(z,t) \tag{6}$$

where $\boldsymbol{e}(z,t) = e(z,t)\boldsymbol{u}_y$ and $\boldsymbol{j}(z,t) = j(z,t)\boldsymbol{u}_y$ are the electric field strength and electric current density oriented perpendicular to $\boldsymbol{b}$ and $\boldsymbol{h}$. The width of the sheet is assumed to be large as compared to the thickness, so that the return paths of the currents at the edges can be neglected. Due to the fixed directions, the field quantities can be handled only as scalar quantities b, h, e, j, respectively. We assume that no net current flows in the laminations and thus, due to symmetry reasons, the magnetic field quantities are symmetric and the electric field quantities are antisymmetric with respect to the middle plane of the lamination: $b(z,t) = b(-z,t)$, $h(z,t) = h(-z,t)$, $e(z,t) = -e(-z,t)$, and $j(z,t) = -j(-z,t)$.

The constitutive laws are

$$j = \sigma e \tag{7}$$

$$h = h_{\mathrm{hy}}(b). \tag{8}$$

Conductivity σ is assumed to be constant in the whole lamination. Equation (8) denotes a hysteretic relationship between the local fields $h(z,t)$ and $b(z,t)$. The hysteresis model, applied

to describe the history-dependent function h_{hy}, is explained in Section III-B.

Combining (5)–(7) yields the following 1-D diffusion equation, which describes the penetration of the magnetic field into the lamination in the presence of eddy currents

$$\frac{\partial^2 h\,(z,t)}{\partial z^2} = \sigma \frac{\partial b\,(z,t)}{\partial t}. \tag{9}$$

Solving this equation together with (8) yields the magnetic flux density and field distributions $b(z,t)$ and $h(z,t)$ from which the hysteresis and eddy-current losses can be derived. Two kinds of boundary conditions can be considered. Either the field strength on the surface of the lamination $h_{\mathrm{s}}(t) = h(\pm\frac{d}{2}, t)$ or the average flux density $b_0(t) = \frac{1}{d}\int_{-d/2}^{d/2} b(z,t)dz$ can be assumed to be known. h_{s} corresponds to the current flowing in the windings around the core according to (1), while b_0 corresponds to the time-integral of the back-electromotive force induced by the flux in the core according to (2). A suitable boundary condition can be chosen based on the application and the type of supply.

In a general nonlinear case, (9) needs to be solved numerically. Accounting for the symmetry, we search for the solution of $b(z,t)$ as a truncated cosine series with n terms

$$b\,(z,t) = \sum_{i\,=\,0}^{n-1} b_i\,(t)\,\alpha_i\,(z) \tag{10}$$

where $\alpha_i(z) = \cos(2\pi i \frac{z}{d})$. Consistently to the notation in the paragraph above, b_0 represents the average flux density in the sheet. Substituting (10) into (9) and integrating twice gives

$$\tilde{h}\,(z,t) = h_{\mathrm{s}}\,(t) - \sigma d^2 \sum_{i\,=\,0}^{n-1} \frac{\partial b_i\,(t)}{\partial t}\beta_i\,(z) \tag{11}$$

where $\beta_i(z,t)$ are such that $\beta_i(\pm\frac{d}{2}) = 0$ and $\alpha_i(z) = -d^2\frac{\partial^2\beta_i(z)}{\partial z^2}$. Together, $b(z,t)$ in (10) and $\tilde{h}(z,t)$ in (11) identically satisfy (9). However, when n is finite, the fields cannot exactly satisfy the constitutive law (8), which is thus expressed weakly with respect to the basis functions α_i

$$\frac{1}{d}\int_{-d/2}^{d/2}\left[\tilde{h}\,(z,t) - h_{\mathrm{hy}}\,(b\,(z,t))\right]\alpha_i\,(z)\,dz = 0. \tag{12}$$

Substituting (11) here, and letting i to vary from 0 to $n-1$ yields a system of n ordinary differential equations

$$\begin{bmatrix} h_{\mathrm{s}}\,(t) \\ 0 \\ \vdots \\ 0 \end{bmatrix} = \frac{1}{d}\int_{-d/2}^{d/2} h_{\mathrm{hy}}\,(b\,(z,t)) \begin{bmatrix} \alpha_0\,(z) \\ \alpha_1\,(z) \\ \vdots \\ \alpha_{n-1}\,(z) \end{bmatrix} dz + \boldsymbol{C}\frac{d}{dt}\begin{bmatrix} b_0\,(t) \\ b_1\,(t) \\ \vdots \\ b_{n-1}\,(t) \end{bmatrix}. \tag{13}$$

The elements of matrix $\boldsymbol{C}$ are given by

$$C_{ij} = \sigma d^2 \frac{1}{d}\int_{-d/2}^{d/2} \alpha_i\,(z)\,\beta_j\,(z)\,dz \tag{14}$$

where the indexing is such that $i, j = 0, \ldots, n-1$. The values are

$$C_{ij} = \begin{cases} \dfrac{\sigma d^2}{12}, & \text{if } i = j = 0 \\ \dfrac{\sigma d^2}{2\pi^2 (i+j)^2}, & \text{if } i = j > 0 \\ \dfrac{\sigma d^2 (-1)^{(i+j+1)}}{4\pi^2 (i+j)^2}, & \text{if } ij = 0 \text{ and } i+j > 0 \\ 0, & \text{otherwise} \end{cases} \tag{15}$$

meaning that only the first row, first column, and the diagonal are nonzero. If $h_{\mathrm{s}}(t)$ is known, $b_0(t), \ldots, b_{n-1}(t)$ can be solved from (13). On the other hand, if $b_0(t)$ is known, the solution of (13) yields $h_{\mathrm{s}}(t)$ and $b_1(t), \ldots, b_{n-1}(t)$.

If only the single term b_0 in the flux-density expansion is considered (meaning that $n = 1$), (13) reduces to

$$h_{\mathrm{s}}\,(t) = h_{\mathrm{hy}}\,(b_0\,(t)) + \frac{\sigma d^2}{12}\frac{db_0\,(t)}{dt} \tag{16}$$

which is usually called a *low-frequency assumption* for eddy-currents. Using (16) means that the skin effect of the eddy-currents in the core laminations is neglected, and the flux density is constant along the thickness. The higher the value of n in (13), the smaller skin depths can be accounted for.

B. Hysteresis and Excess Loss Models

The relationship between the local magnetic field strength and flux density is hysteretic and denoted $h(z,t) = h_{\mathrm{hy}}(b(z,t))$, where h_{hy} is a function which preserves the history of its input argument. The hysteretic behavior is modeled with the HDHM described in detail in [28]. In brief, the HDHM approximates the shape of the first order reversal curves (FORCs) based on the shape of the major hysteresis loop. The model can be identified from a single branch of the major loop (ascending branch $h = h_{\mathrm{a}}(b)$ or descending branch $h = h_{\mathrm{d}}(b)$) in a chosen interval $b \in [-b_{\mathrm{T}}, b_{\mathrm{T}}]$, where hysteresis is considered and a single-valued curve $h_{\mathrm{sv}}(b)$ is used when $|b| > b_{\mathrm{T}}$. Functions $h_{\mathrm{a}}(b)$, $h_{\mathrm{d}}(b)$, and $h_{\mathrm{sv}}(b)$ can be conveniently expressed as splines.

We identified the HDHM for Nippon 35H300 electrical steel based on the magnetization curve found in the manufacturer catalog [36]. The ascending major loop branch $h_{\mathrm{a}}(b)$ was expressed as a linear spline with 101 nodes below $b_{\mathrm{T}} = 1.5$ T. Fig. 4 shows the major loop digitized from [36], as well as the modeled major loop and some FORCs and minor loops. The single-valued curve $h_{\mathrm{a}}(b)$ above $b_{\mathrm{T}} = 1.5$ T was expressed with a linear spline with 100 nodes.

Following the approach presented in [34], the excess losses are added as a rate-dependent contribution

$$h_{\mathrm{ex}}\,(t) = c_{\mathrm{ex}}\left|\frac{db_0}{dt}\right|^{-0.5}\frac{db_0}{dt} \tag{17}$$

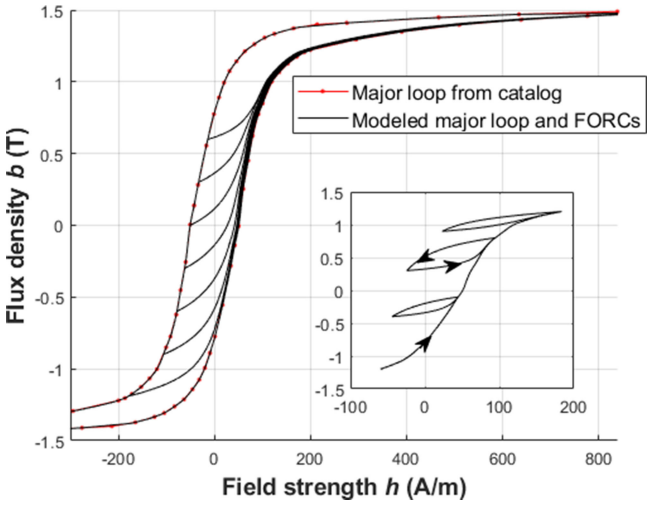

Fig. 4. Major hysteresis loop for Nippon 35H300 electrical steel digitized from the manufacturer catalog as well as the major loop and a set of ascending first-order reversal curves obtained from the history-dependent hysteresis model. The inset shows some simulated minor loops.

to $h_s(t)$ in (13) or (16). An excess loss coefficient of $c_{ex} = 0.314\ \mathrm{W/m^3(s/T)^{1.5}}$ was identified from the core-loss curve found in the manufacturer catalog [36]. Details on the fitting of the hysteresis and excess loss coefficients are discussed in the Appendix.

C. Iron Losses

After the 1-D flux-density distribution in the lamination thickness has been solved from (13), it can be used to derive the eddy current and hysteresis loss-density distributions in the lamination. The instantaneous eddy-current loss density per unit mass averaged over the lamination thickness is given by

$$p_{cl}(t) = \frac{1}{\rho}\left(\frac{d\boldsymbol{b}(t)}{dt}\right)^{\mathrm{T}} \boldsymbol{C}\frac{d\boldsymbol{b}(t)}{dt} \tag{18}$$

where the column vector $\boldsymbol{b}(t)$ contains the coefficients $b_i(t)$, $i = 0, \ldots, n-1$. The instantaneous magnetization power averaged over the thickness is given by

$$p_{hy}(t) = \frac{1}{\rho d}\int_{-d/2}^{d/2} h_{hy}(z,t)\frac{\partial b(z,t)}{\partial t}dz. \tag{19}$$

The excess losses are obtained as

$$p_{ex}(t) = \frac{c_{ex}}{\rho d}\int_{-d/2}^{d/2}\left|\frac{db_0(t)}{dt}\right|^{1.5} dz. \tag{20}$$

While p_{cl} and p_{ex} are always greater than zero and represent the instantaneous loss dissipation, p_{hy} contains both hysteresis losses and reactive power and thus also obtains negative values. Time-average losses are obtained by averaging $p_{cl}(t)$, $p_{hy}(t)$, and $p_{ex}(t)$ over a closed cycle of magnetization. The total iron loss is the sum of the averaged eddy-current, hysteresis, and excess losses.

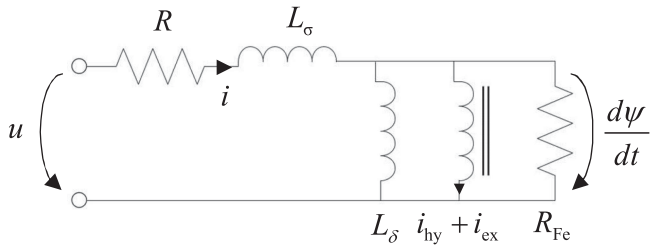

Fig. 5. Equivalent circuit of an inductor with an air gap and an iron core with hysteresis, eddy-current, and excess losses.

IV. Inductor Model in Simulink

A. Voltage Equations

Although the test inductor does not have an air gap, we derive the voltage equations in a general form so that an air gap can also be considered, if needed. The toroidal inductor is modeled with a simple reluctance network model. The voltage equation of the test inductor can be written as follows:

$$u = Ri + L_\sigma\frac{di}{dt} + \frac{d\psi}{dt} \tag{21}$$

where u is the primary voltage, i is the primary current, ψ is the primary flux linkage, and R and L_σ are the primary resistance and leakage inductance, respectively. The equivalent circuit is shown in Fig. 5. The three current branches will be derived in Section IV-B.

The current and flux linkages are related to the surface field strength and the average flux density as follows:

$$i = \frac{l_{Fe}}{N_1}h_s + \frac{\delta}{\mu_0 N_1}\frac{A_{Fe}}{A_\delta}b_0 \tag{22}$$

$$\psi = N_1 A_{Fe} b_0 \tag{23}$$

where l_{Fe} and δ are the lengths of the flux paths in the iron core and the air gap, respectively, A_{Fe} and A_δ are the corresponding cross-sectional areas through which the flux flows and μ_0 is the permeability of free space. Implementing the relationship of h_s and b_0 through (13) allows eddy-current and hysteresis effects to be accounted for in the circuit simulation of the inductor.

Equations (13), (16), (22), and (23) were implemented in Simulink in order to simulate the toroid with PWM converter supply similarly to the measurements. Separate Simulink models were implemented for the cases $n = 0$ and $n > 0$. The implementation details are discussed next.

B. Model Without Skin Effect

Adding (17) to (16) and substituting the result in place of h_s in (22) yields

$$i = \frac{\delta}{\mu_0 N_1}\frac{A_{Fe}}{A_\delta}b_0 + \frac{l_{Fe}}{N_1}\left(h_{hy}(b_0) + c_{ex}\left|\frac{db_0}{dt}\right|^{-0.5}\frac{db_0}{dt}\right) + \frac{l_{Fe}}{N_1}\frac{\sigma d^2}{12}\frac{db_0}{dt} \tag{24}$$

which means that the primary current is divided into three parallel branches (see Fig. 5): the first one corresponding to the

magnetomotive force (mmf) or the air gap, the second one to the mmf and excess loss of the iron core, and the last one to the eddy-current loss. Solving b_0 from (23) and substituting this into (24) yields

$$i = \underbrace{\frac{\delta}{\mu_0 N_1^2 A_\delta}}_{L_\delta^{-1}} \psi + \underbrace{\frac{l_{\mathrm{Fe}}}{N_1} h_{\mathrm{hy}}\left(\frac{\psi}{N_1 A_{\mathrm{Fe}}}\right)}_{i_{\mathrm{hy}}} + \underbrace{\frac{l_{\mathrm{Fe}} c_{\mathrm{ex}}}{\sqrt{N_1^3 A_{\mathrm{Fe}}}} \left|\frac{d\psi}{dt}\right|^{-0.5} \frac{d\psi}{dt}}_{i_{\mathrm{ex}}} + \underbrace{\left(\frac{l_{\mathrm{Fe}}}{N_1^2 A_{\mathrm{Fe}}} \frac{\sigma d^2}{12}\right)}_{R_{\mathrm{Fe}}^{-1}} \frac{d\psi}{dt} \tag{25}$$

where the coefficient of the first term is the inverse of the air-gap inductance L_δ, and the last term represents an eddy-current-loss resistance placed in parallel with the magnetization branch. It is observed that if $c_{\mathrm{ex}} \neq 0$, the excess-losses could be lumped into the same resistance R_{Fe}, but this would become dependent on the value of the rate-of-change of the flux linkage. We thus prefer to consider the excess loss as an additional contribution to the magnetization current along with i_{hy}. Although the equivalent circuit in Fig. 5 shows an inductance for the middle branch, it is emphasized that the two middle terms of (25) cannot be reasonably represented by an inductance, since $\psi/(i_{\mathrm{hy}} + i_{\mathrm{ex}}) \in (-\infty, \infty)$ due to the hysteretic and rate-dependent relationship.

The voltage equation (21) together with the flux-current relationship (25) is implemented in MATLAB R2016b using Simulink's Simscape Power Systems environment.[1] The implementation is illustrated in Fig. 6(a) and some explanations are given in Table II. The HDHM was implemented as a Fortran code which was interfaced with the Simulink model through a C-MEX Gateway function. Components R, L_δ, and R_{Fe} are implemented as Simscape Power Systems Specialized Technology blocks. The first two leftmost branches of Fig. 5 corresponding to the magnetization current are implemented with a controlled current source, whose value is calculated using the "HDHM"-block and the excess-loss coefficient. The voltage between input terminals 1 and 2 is equal to u.

C. Model With Skin Effect

Derivation of the model equations accounting for the skin effect is slightly more complex. To simplify the notation, we separate matrix $\boldsymbol{C}$ of (13) into four blocks as follows:

$$\boldsymbol{C} = \begin{bmatrix} C_{00} & \boldsymbol{C}_{0,1:} \\ \boldsymbol{C}_{1:,0} & \boldsymbol{C}_{1:,1:} \end{bmatrix}. \tag{26}$$

The notation means that, for example, $\boldsymbol{C}_{0,1:} = [C_{0,1} \ldots C_{0,n-1}]$. The sizes of $\boldsymbol{C}_{0,1:}$, $\boldsymbol{C}_{1:,0}$, and $\boldsymbol{C}_{1:,1:}$ are $1 \times n-1$, $n-1 \times 1$, and $n-1 \times n-1$, respectively. Similar notations $\boldsymbol{b}_{1:}$ and $\boldsymbol{\alpha}_{1:}$ are used to denote the higher order flux-density components $[b_1 \ldots b_{n-1}]^{\mathrm{T}}$ and skin-effect basis functions $[\alpha_1 \ldots \alpha_{n-1}]^{\mathrm{T}}$.

Similarly to the Section IV-B, we start by solving h_{s} from the first row of (13), adding (17), and substituting the result into

[1]The models are available at https://github.com/prasilo/simulink-pwm-inductor/tree/v1.0.

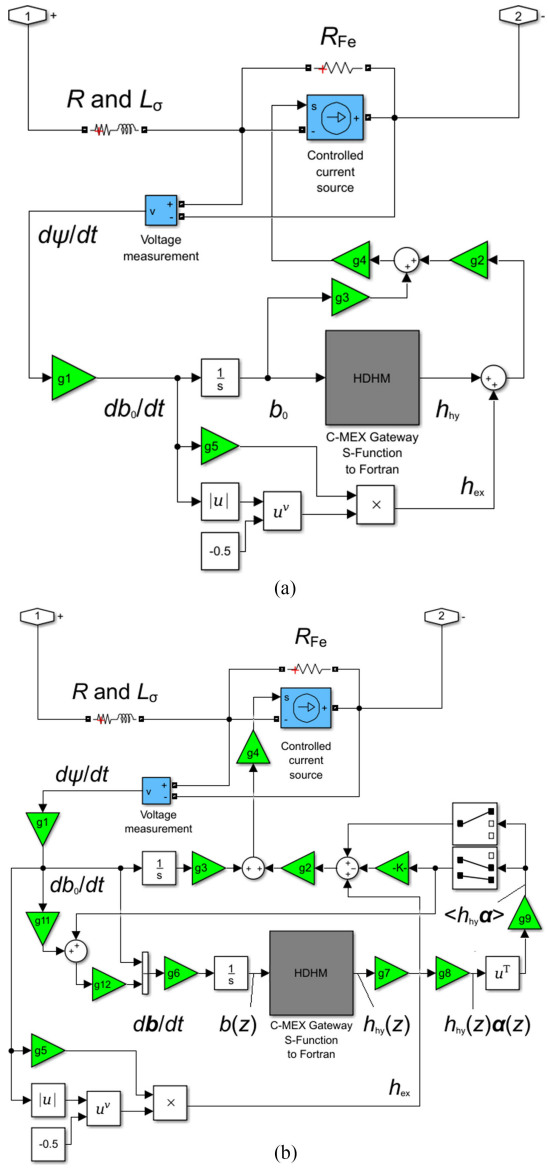

Fig. 6. Illustration of the Simulink implementations of the inductor model (a) without and (b) with skin effect. Notation $\langle\cdot\rangle$ denotes averaging over the lamination thickness $z \in [-d/2, d/2]$. The gains are explained in Table II. The paths producing h_{ex} result in algebraic loops.

(22), which yields

$$i = \frac{\psi}{L_\delta} + \frac{l_{\mathrm{Fe}}}{N_1}\frac{1}{d}\int_{-d/2}^{d/2} h_{\mathrm{hy}}\alpha_0 dz + \frac{l_{\mathrm{Fe}}}{N_1} c_{\mathrm{ex}} \left|\frac{db_0}{dt}\right|^{-0.5} \frac{db_0}{dt} + \frac{l_{\mathrm{Fe}}}{N_1}\left(C_{00}\frac{db_0}{dt} + \boldsymbol{C}_{0,1:}\frac{d\boldsymbol{b}_{1:}}{dt}\right). \tag{27}$$

Next, we solve $d\boldsymbol{b}_{1:}/dt$ from the other rows of (13) as follows:

$$\frac{d\boldsymbol{b}_{1:}}{dt} = -\boldsymbol{C}_{1:,1:}^{-1}\left(\frac{1}{d}\int_{-d/2}^{d/2} h_{\mathrm{hy}}\boldsymbol{\alpha}_{1:} dz + \boldsymbol{C}_{1:,0}\frac{db_0}{dt}\right) \tag{28}$$

TABLE II
EXPLANATIONS OF THE GAIN BLOCKS IN FIG. 6

GAIN	EXPRESSION	DESCRIPTION
g1	$1/(N_1 A_{\mathrm{Fe}})$	Scales ψ to b_0.
g2	l_{Fe}	Scales h_{s} to the mmf of the iron core.
g3	$\delta A_{\mathrm{Fe}}/(\mu_0 A_\delta)$	Scales b_0 to the mmf of air.
g4	$1/N_1$	Scales mmf to primary current.
g5	c_{ex}	Excess loss coefficient.
g6	$\boldsymbol{A}$ $A_{ji} = \alpha_i(z_j)$	Matrix multiplication from left. Performs summation in (10) for all z_j, $j = 1, \ldots, m$.
g7	[1 1 … 1] (n elements)	Matrix multiplication from right. Replicates column vector $h_{\mathrm{hy}}(z_j)$ n times.
g8	$\boldsymbol{A}$ $A_{ji} = \alpha_i(z_j)$	Elementwise matrix multiplication. Scales $h_{\mathrm{hy}}(z_j)$ to $h_{\mathrm{hy}}(z_j)\alpha_i(z_j)$ for $i = 0,\ldots, n–1$ and $j = 1, \ldots, m$.
g9	$\boldsymbol{w}$	Matrix multiplication from right. Yields the weighted sum of $h_{\mathrm{hy}}(z_j)\alpha_i(z_j)$ over $j = 1, \ldots, m$.
g10	$\boldsymbol{C}_{0,\mathrm{k}}\boldsymbol{C}_{\mathrm{k},\mathrm{k}}^{-1}$	Matrix multiplication from left. Third term in (30).
g11	$\boldsymbol{C}_{\mathrm{k},0}$	Second term in (28)
g12	$-\boldsymbol{C}_{\mathrm{k},\mathrm{k}}^{-1}$	Multilplier on the right-hand-side of (28)

and substitute these in (27)

$$i = \frac{\psi}{L_\delta} + \frac{l_{\mathrm{Fe}}}{N_1}\frac{1}{d}\int_{-d/2}^{d/2} h_{\mathrm{hy}}\alpha_0\,dz - \frac{l_{\mathrm{Fe}}}{N_1}\boldsymbol{C}_{0,1:}\boldsymbol{C}_{1:,1:}^{-1} \times \frac{1}{d}\int_{-d/2}^{d/2} h_{\mathrm{hy}}\boldsymbol{\alpha}_{1:}\,dz + \frac{l_{\mathrm{Fe}}}{N_1}c_{\mathrm{ex}}\left|\frac{db_0}{dt}\right|^{-0.5}\frac{db_0}{dt} + \frac{l_{\mathrm{Fe}}}{N_1}\left(C_{00} - \boldsymbol{C}_{0,1:}\boldsymbol{C}_{1:,1:}^{-1}\boldsymbol{C}_{1:,0}\right)\frac{db_0}{dt}. \tag{29}$$

Finally, substituting b_0 from (23) results in

$$i = \frac{\psi}{L_\delta} + \underbrace{\frac{l_{\mathrm{Fe}}}{N_1}\frac{1}{d}\int_{-d/2}^{d/2} h_{\mathrm{hy}}\alpha_0\,dz - \frac{l_{\mathrm{Fe}}}{N_1}\boldsymbol{C}_{0,1:}\boldsymbol{C}_{1:,1:}^{-1}\frac{1}{d}\int_{-d/2}^{d/2} h_{\mathrm{hy}}\boldsymbol{\alpha}_{1:}\,dz}_{i_{\mathrm{hy}}} + \underbrace{\frac{l_{\mathrm{Fe}}c_{\mathrm{ex}}}{\sqrt{N_1^3 A_{\mathrm{Fe}}}}\left|\frac{d\psi}{dt}\right|^{-0.5}\frac{d\psi}{dt}}_{i_{\mathrm{ex}}} + \underbrace{\frac{l_{\mathrm{Fe}}}{N_1^2 A_{\mathrm{Fe}}}\left(C_{00} - \boldsymbol{C}_{0,1:}\boldsymbol{C}_{1:,1:}^{-1}\boldsymbol{C}_{1:,0}\right)}_{R_{\mathrm{Fe}}}\frac{d\psi}{dt}. \tag{30}$$

It is seen that inclusion of the skin effect causes additional terms in i_{hy} as well as the eddy-current loss resistance R_{Fe}. In addition, since $b(z,t)$ and thus $h_{\mathrm{hy}}(b(z,t))$ are not constant along the lamination thickness, the integrations in (28) and (30) need to be carried out numerically. This is done using a set of m Gauss integration points z_j and weights w_j, $j = 1, \ldots, m$. Functions $\alpha_i(z)$, $i = 0, \ldots, n-1$, $b(z,t)$, and $h_{\mathrm{hy}}(b(z,t))$ are evaluated in these Gauss points z_j and the integrations in (28) and (30) are obtained as the sum of the integrands weighted with w_j. The values of $\alpha_i(z_j)$ are assembled into an $m \times n$ matrix $\boldsymbol{A}$ such that $A_{ji} = \alpha_i(z_j)$, and the weights are assembled in a column vector $\boldsymbol{w}$. Simulink implementation of the voltage equation (21) together with (28) and (30) is demonstrated in Fig. 6(b) and Table II. Inclusion of the excess losses makes (25) and (30) implicit with respect to $d\psi/dt$, which causes algebraic loops to the simulation model. This might slow down the simulation or cause convergence problems in some cases. However, in the simulations considered in this paper, no problems were observed.

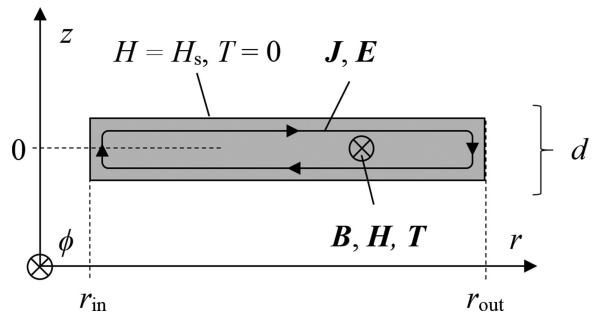

Fig. 7. Problem setting for the axisymmetric FE problem.

V. AXISYMMETRIC FE MODEL

An axisymmetric 2-D FE model for a single lamination is also developed in order to verify that the 1-D approaches described in Sections III and IV are valid for the considered toroidal inductor. Fig. 7 shows the geometry in a cylindrical $r\phi z$-coordinate system, z being the symmetry axis. Capital letters are used here to denote the 2-D dependency of the quantities contrary to Section III. An electric vector potential $\boldsymbol{T}(r,z,t) = T(r,z,t)\boldsymbol{u}_\phi$ and a magnetic scalar potential $\Omega(\phi,t) = F(t)\phi/(2\pi)$ are considered such that the magnetic field strength becomes $\boldsymbol{H}(r,z,t) = \boldsymbol{T}(r,z,t) + \nabla\Omega(\phi,t) = (T(r,z,t) + H_{\mathrm{s}}(r,t))\boldsymbol{u}_\phi = H(r,z,t)\boldsymbol{u}_\phi$. The offset $H_{\mathrm{s}}(r,t) = F(t)/(2\pi r)$ is inversely proportional to the radial coordinate and equals the surface value of H when a homogeneous Dirichlet condition is set for T on the surfaces of the sheet,

$F(t) = N_1 i(t)$ corresponding to the magnetomotive force created by the primary winding.

Combining Ampere's and Faraday's laws in the axisymmetric case yields

$$-\frac{\partial^2 T}{\partial z^2} - \frac{\partial}{\partial r}\left(\frac{1}{r}\frac{\partial (rT)}{\partial r}\right) + \sigma \frac{\partial b_{\text{hy}}(H)}{\partial t} = 0. \tag{31}$$

Solution of (31) by the FE method would be straightforward if a material model was available in the form $B = b_{\text{hy}}(H)$ and if the current *i*(*t*) was used as the source to the problem. In our case, however, the material model is available only in the inverse form $H = h_{\text{hy}}(B)$, and we also need to use an integral condition for *B* in order to supply the desired average flux density $b_0(t)$ as the source to the FE problem. We thus choose *B* as an additional variable and end up with a system

$$-\frac{\partial^2 T}{\partial z^2} - \frac{\partial}{\partial r}\left(\frac{1}{r}\frac{\partial (rT)}{\partial r}\right) + \sigma \frac{\partial B}{\partial t} = 0 \tag{32}$$

$$T + \frac{F}{2\pi r} = h_{\text{hy}}(B) + c_{\text{ex}}\left|\frac{\partial B}{\partial t}\right|^{-0.5}\frac{\partial B}{\partial t} \tag{33}$$

$$\frac{1}{d(r_{\text{out}} - r_{\text{in}})}\int_{-d/2}^{d/2}\int_{r_{\text{in}}}^{r_{\text{out}}} B dr dz = b_0. \tag{34}$$

Equation (32) describes the field problem, while (33) enforces the constitutive law, which includes the hysteresis and excess losses. Equation (34) forces the average flux density $b_0(t)$ into the sheet. From (32)–(34) the distributions of *T* and *B* and the scalar-valued *F* can be solved for a given $b_0(t)$.

Equation (32) is discretized using test functions $\tilde{T}$ which results into the weak form

$$\int_{-d/2}^{d/2}\int_{r_{\text{in}}}^{r_{\text{out}}} r\left[\frac{\partial \tilde{T}}{\partial z}\frac{\partial T}{\partial z} + \left(\frac{\tilde{T}}{r} + \frac{\partial \tilde{T}}{\partial r}\right)\left(\frac{T}{r} + \frac{\partial T}{\partial r}\right) + \sigma \tilde{T}\frac{\partial B}{\partial t}\right] dr dz = 0 \tag{35}$$

and *B* is evaluated in the 2-D Gauss integration points. For symmetry reasons, only the upper half of the lamination $0 \le z \le d/2$ needs to be simulated. This upper half is divided into 890 quadratic triangular elements with 1969 nodes and three integration points per element. After the solution, the instantaneous magnetization power and the eddy-current and excess losses are averaged over the lamination volume $V = \pi(r_{\text{out}}^2 - r_{\text{in}}^2)d$ as

$$p_{\text{hy}}(t) = \frac{2\pi}{\rho V}\int_{r_{\text{in}}}^{r_{\text{out}}}\int_{-d/2}^{d/2} r h_{\text{hy}}(B)\frac{\partial B}{\partial t} dz dr \tag{36}$$

$$p_{\text{cl}}(t) = \frac{2\pi}{\rho V \sigma}\int_{r_{\text{in}}}^{r_{\text{out}}}\int_{-d/2}^{d/2} r\|\nabla T\|^2 dz dr \tag{37}$$

$$p_{\text{ex}}(t) = \frac{2\pi c_{\text{ex}}}{\rho V}\int_{r_{\text{in}}}^{r_{\text{out}}}\int_{-d/2}^{d/2} r\left|\frac{\partial B}{\partial t}\right|^{1.5} dz dr. \tag{38}$$

Time-averaged losses are obtained by averaging (36)–(38) over a closed cycle of magnetization.

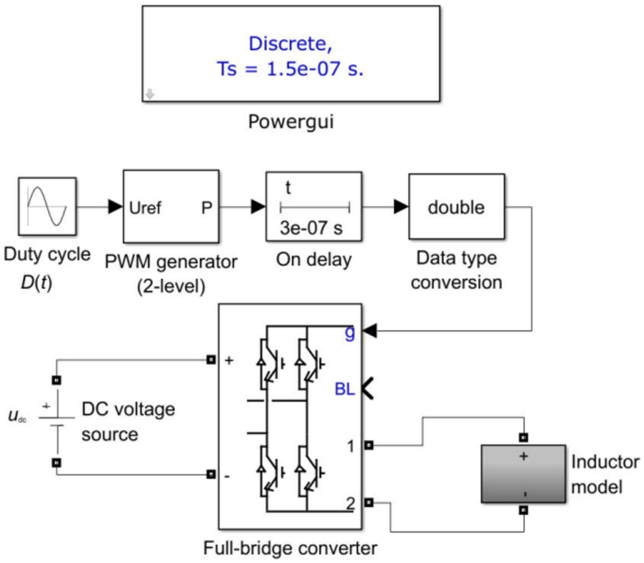

Fig. 8. Model for the PWM full-bridge converter supplying the inductor for simulating the measurement conditions. In this case the deadtime is 300 ns and maximum time-step length 150 ns.

VI. Application and Results

A. Supply Circuit and Time-Stepping

The Simulink inductor model is supplied by voltage *u* imposed over the input terminals 1 and 2 in Fig. 6. Sinusoidal supply voltages and other waveforms can be straightforwardly imposed by Simscape "Controlled voltage source"-blocks. In order to replicate the measurement conditions for the toroidal test inductor supplied with PWM voltages with deadtime, the built-in converter models are used. Fig. 8 illustrates the implementation. The duty cycle *D*(*t*) is compared to a carrier wave with frequency f_s / 2 in the "PWM generator"-block and the rising edge of each generated pulse is delayed by the deadtime using the "On delay"-block. The built-in "Full-bridge converter"-block is used for producing the PWM voltage which is fed to the inductor model. It is emphasized that when the deadtime is accounted for, the voltage *u* supplied to the inductor becomes dependent on the current due to the load commutation during the deadtime. Coupling the inductor model to a circuit simulator is thus essential in order to account for the effects of the deadtime on the losses.

The continuous-time solver *ode45* was used in Simulink for the time-integrations. However, for the Simscape Power Systems Specialized Technology blocks a discrete Backward-Euler (BE) solver was applied. This was observed to greatly improve the convergence. In the PWM simulations the maximum time-step size for the *ode45* solver and the fixed time-step of the BE solver was set to 150 ns, corresponding to half of the 300 ns deadtime.

B. Analytical Validation

The eddy-current model (13) has been validated in [24] by comparison to a 1-D FE model. However, since the Simulink implementation is rather complex, we quickly validate the

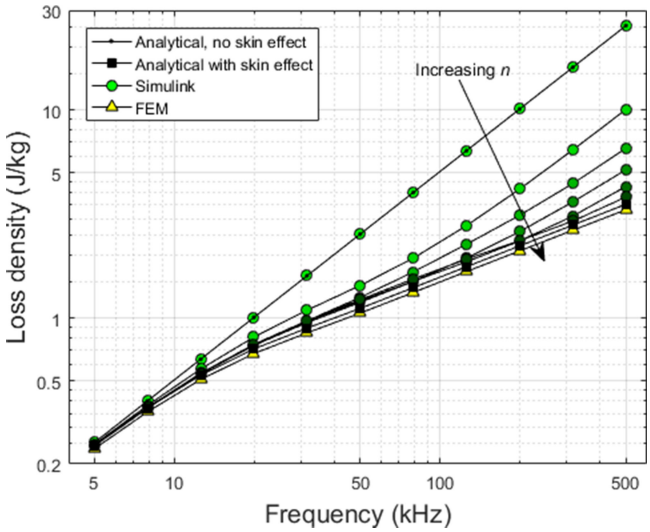

Fig. 9. Validation of the eddy-current loss model implementation in Simulink by comparing simulated energy-loss densities with $n = 1, 2, 3, 4, 5, 6$ skin-effect terms to (39) with and without $X(x)$ at different frequencies of a sinusoidal average flux density $b_0(t)$. Finite-element simulation results are also shown.

implementation by comparing to an analytical eddy-current loss model. The resistance and leakage inductance are set to zero ($R = L_\sigma = 0$) so that the voltage becomes $u(t) = A_{\mathrm{Fe}} N_1 \cdot db_0(t)/dt$ and thus we can obtain a sinusoidal $b_0(t) = b_{\max} \cdot \sin(2\pi f t)$ by imposing $u(t) = 2\pi f A_{\mathrm{Fe}} N_1 b_{\max} \cdot \cos(2\pi f t)$. If the excess losses are omitted and the hysteretic relationship is replaced by a constant reluctivity ν so that $h_{\mathrm{hy}}(b(z,t)) = \nu b(z,t)$, the eddy-current loss density can be obtained analytically as

$$p_{\mathrm{cl}} = \frac{\sigma d^2 f^2 \pi^2}{6\rho} b_{\max}^2 X(x) \text{ with } X(x) = \frac{3}{x} \frac{\sinh x - \sin x}{\cosh x - \cos x} \tag{39}$$

where $x = d(\pi f \sigma/\nu)^{1/2}$ and term $X(x)$ accounts for the skin effect [37]. Fig. 9 compares the simulated energy-loss densities p_{cl}/f with a relative permeability of 1000 to (39) with and without the $X(x)$ term at $b_{\max} = 1$ T and different fundamental frequencies f. When the number of skin-effect terms in the flux-density expansion (10) is $n = 1$, meaning that the skin-effect is neglected, the simulated losses correspond accurately to (39) without $X(x)$. When n is increased, the losses approach (39) with $X(x)$, which validates the implementation. Results simulated with the axisymmetric FE model under similar conditions are also shown, and correspond well to the ones predicted by (39) with $X(x)$.

In [38], a theoretical expression is derived for the additional PWM-induced eddy-current losses when changing from sinusoidal supply voltage $u(t) = a \cdot u_{\mathrm{dc}} \cdot \cos(2\pi f t)$ to full-bridge PWM converter with duty cycle $D(t) = a \cdot \sin(2\pi f t)$

$$\frac{\Delta p_{\mathrm{cl}}(a)}{\Delta p_{\mathrm{cl}}\left(\frac{2}{\pi}\right)} = \pi a \left(1 - \frac{\pi}{4} a\right). \tag{40}$$

The expression is normalized with the maximum occurring at $a = 2/\pi$ and yields the exact loss, provided again that $R = L_\sigma = 0$, skin effect is neglected, and that the loss

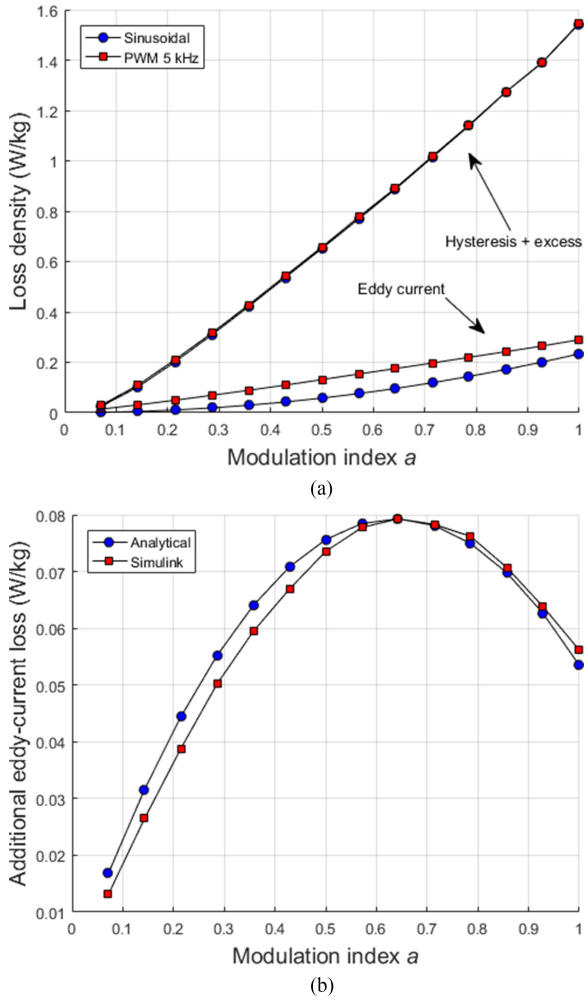

Fig. 10. (a) Hysteresis, excess, and eddy-current losses at PWM and sinusoidal supplies. (b) Comparison of the additional PWM-induced eddy-current loss to the theoretical model (40).

occurring during one switching cycle is independent of the input current value. The Simulink model was verified against (40), by simulating the losses at $f_{\mathrm{s}} = 5$ kHz PWM supply and different modulation indices a, and comparing these to sinusoidal supply. The dc-link voltage was kept at $u_{\mathrm{dc}} = 9$ V, the fundamental frequency was $f = 50$ Hz, and the number of skin-effect terms was $n = 2$. Fig. 10(a) shows the hysteresis, excess, and eddy-current losses at different values of a under both sinusoidal and PWM supplies. The sum of the hysteresis and excess losses remains almost unchanged independent of the supply. The eddy-current losses are smaller to the hysteresis losses due to the low fundamental frequency, but they are significantly affected by the PWM supply. Fig. 10(b) shows the PWM-induced additional eddy-current loss and compares this to (40), which has been scaled to the same maximum as the simulated loss increase. The simulation results correspond well to the theoretical model.

C. Comparison to Measurements

The developed Simulink model is next used to replicate the measurement conditions for the toroidal test inductor. The duty

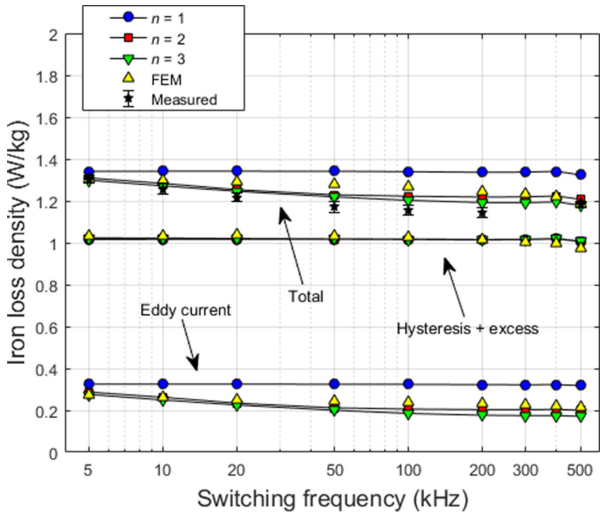

(a)

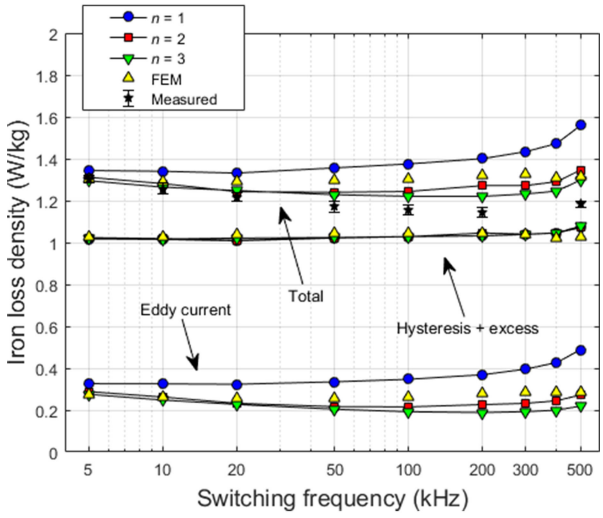

(b)

Fig. 11. Simulated iron-loss densities with different switching frequencies and different numbers of skin-effect terms *n*. (a) without deadtime and (b) with deadtime of 300 ns. FE simulation results and measured losses with error in the case of 300 ns deadtime are also shown.

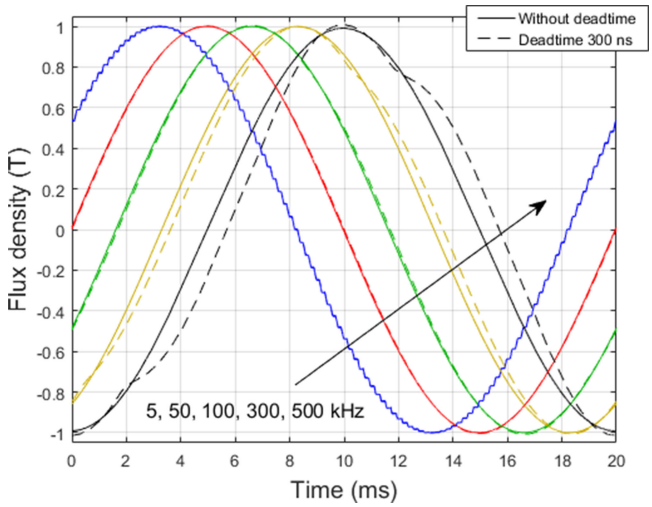

Fig. 12. Simulated flux-density waveforms at 5, 50, 100, 300, and 500 kHz switching frequencies both without and with deadtime when $n = 3$.

cycle $D(t) = a \cdot \sin(2\pi f t)$ is a sinusoidal signal with a modulation ratio of $a = 0.5$ and fundamental frequency of $f = 50$ Hz. Switching frequencies ranging from $f_s = 5$ to 500 kHz are considered. Like in the measurements, the value of the dc-link voltage is iterated until a flux-density amplitude of 1 T is reached. The average flux-density waveforms $b_0(t)$ obtained from the Simulink models are then used as sources to the 2-D FE problem. The same operation points are simulated over two full cycles of $b_0(t)$ using a time-step of 300 ns, resulting in around 133 000 time steps in total. On average, one FE simulation takes roughly 9 h. The Simulink runs take 40 –140 s for two cycles.

Fig. 11(a) shows the simulated iron-loss densities in the case that deadtime is not considered and compares the results to the measurements performed with a deadtime of 300 ns. Results with different numbers of skin-effect terms *n* are shown. The hysteresis losses are rather constant independently of the switching frequency and *n*. On the other hand, the eddy-current losses can be seen to be rather significantly affected by consideration of the skin effect. When the skin effect is not considered ($n = 1$), the eddy-current losses and total losses remain almost constant when the switching frequency increases. However, when the skin effect is accounted for, the eddy-current losses decrease with increasing switching frequency. This effect is visible also in the measurements below $f_s = 200$ kHz. The difference between $n = 2$ and $n = 3$ is rather small. The eddy-current losses simulated with the FE model show a slightly smaller decrease as a function of the switching frequency. However, the overall agreement between the Simulink and FE results is good.

The simulation results with 300 ns deadtime are shown in Fig. 11(b). Up to $f_s = 200$ kHz the simulated losses behave very similarly to those in (a) and are thus not notably affected by the deadtime. However, when the switching frequency exceeds 300 kHz, the eddy-current losses start increasing. The trend in the total losses is rather similar to the measurements, which seems to imply that the increase in the losses at high switching frequencies is caused by the deadtime. However, a close look at the simulated flux-density waveforms in Fig. 12 reveals that the increase in the losses is caused by deforming flux-density waveforms at high switching frequencies when the deadtime is considered. Inspection of the current waveforms in Fig. 13 reveals that the deformation is caused by zero-current clamping (ZCC), which occurs when the primary current drops to zero during deadtime. When the current is zero and all switches are open, there is no voltage which could change the current, which thus remains zero until the deadtime is over. Fig. 13 also shows that when deadtime is considered, the dc-link voltage has to be increased to close to 20 V in order to maintain the flux-density amplitude of 1 T.

The ZCC and the flux-density deformation were not observed during the measurements, and the dc link voltage remained close to 15 V at all switching frequencies. This might be due to the parasitic capacitances, which were not accounted for in the simulations, but which may affect the behavior of the system during the deadtime, as discussed in [39]. This is also suggested by the

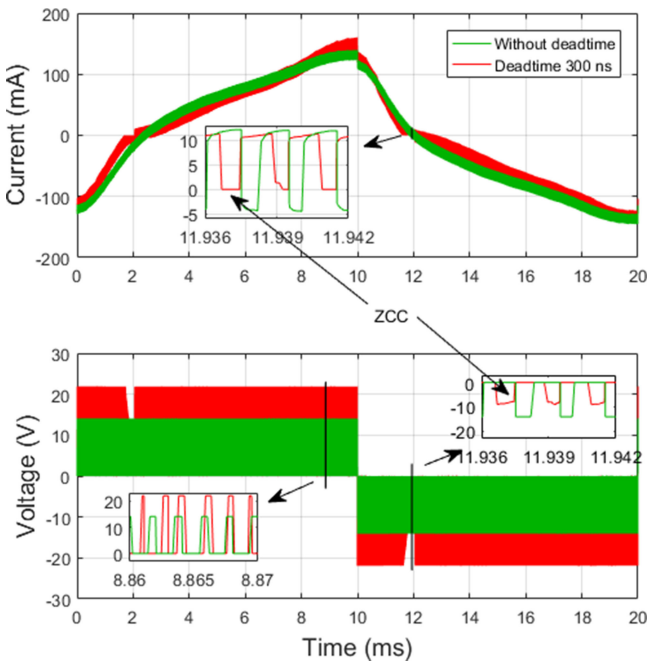

Fig. 13. Simulated primary current and voltage waveforms at 500 kHz switching frequency both without and with deadtime when $n = 3$. The insets show the ZCC when the deadtime is accounted for.

fact that the measured input current total harmonic distortion (THD) varies from 35 to 67%, increasing with the switching frequency, while in the simulations the THD varies from 22 to 27%. In the measurements, the parasitic capacitances and fast switching voltage transients lead to large current spikes and increase the THD [34]. The ZCC and flux-density deformation seem to occur in the measurements of [40] performed up to 190 kHz switching frequency on a different setup. In [40, Figs. 15 and 18], it can be seen that the dc link voltage increases significantly with switching frequency and that the hysteresis loop deforms when the field strength (and thus current) is close to zero when 400 ns deadtime is used.

VII. Discussion and Conclusion

A novel implementation of hysteresis, eddy-current, and excess loss models for laminated magnetic cores in the MATLAB / Simulink environment was presented. The model can be easily coupled to Simscape models for simulating inductors and transformers coupled with complex power-electronics circuits. The model can be used for designing and analyzing, for example, LCL filters or inductors for dc/dc converters. Although a simple single-reluctance model was used in this paper for the toroidal test inductor, the model is not limited to such cases, but can be used in any devices which can be modeled with reluctance networks. In case of toroids with a large width-to-diameter ratio, several parallel flux paths might need to be considered.

The model was validated by replicating the measurement conditions for the GaN FET -inverter supplied toroid in Simulink. When the deadtime was accounted for in the simulations, the average difference between the measured and simulated losses was 3.3%. Taking into account that the iron-loss model was identified merely based on values and curves found from manufacturer catalog data, and that the built-in Simulink blocks were used to replicate the measurements, the agreement between the measurement and simulation results can be considered good. Similar losses were produced by the 2-D axisymmetric FE model.

Accounting for the skin effect of the eddy-currents was found to be important in order to correctly model the decreasing eddy-current losses when the switching frequency increased from 5 to 200 kHz. It appears that above 300 kHz switching frequency, the ZCC causes deformation of the simulated flux density, which was not observed during the measurements. The nonsinusoidal shape of the flux density may lead to overestimation of the iron losses. As discussed in [39], consideration of the parasitic capacitances may be important to correctly model the behavior of the system during the deadtime. This is an interesting topic for future research. However, both the measurement and simulation results presented in this paper imply that laminated-core toroids are a feasible choice also for 100-kHz range switching frequency applications since the losses are not significantly affected by the switching frequency.

Appendix

Some details on the loss model parameter fitting based on the manufacturer catalog [36] are discussed. The figure in [36, pp. 22 and 23] gives a typical core loss curve and the dc hysteresis curve for 35H300. The dc hysteresis curve given at a peak flux density of 1.5 T was first digitized from the pdf. The digitized loop gives a static hysteresis loss of 0.0468 J/kg. However, if the core loss curve given in [36, pp. 22] is divided by the frequency and extrapolated to zero frequency, a static hysteresis loss of $w_{\mathrm{hy}} = 0.0360\,\mathrm{J/\,kg}$ is obtained. This is about 23% lower than predicted by the loop. In order to avoid overestimating the iron losses, the field strength values obtained after digitizing the dc hysteresis curves were reduced by 23% before implementing them in the hysteresis model.

The total core loss at a frequency of $f = 50$ Hz and amplitude $b_{\max} = 1.5\,\mathrm{T}$ was then interpolated from the curve of [36, pp. 22], and the eddy-current loss in this point was estimated analytically with (39) neglecting $X(x)$. The excess loss coefficient was then calculated as follows:

$$c_{\mathrm{ex}} = \rho \frac{p_{\mathrm{tot}} - w_{\mathrm{hy}} f - \frac{\sigma d^2 f^2 \pi^2}{6\rho} b_{\max}^2}{(2\pi f b_{\max})^{1.5}} \tag{41}$$

yielding $c_{\mathrm{ex}} = 0.314\,\mathrm{W/\,m^3(s/\,T)^{1.5}}$.

References

[1] J. Szynowski, R. Kolano, A. Kolano-Burian, and M. Polak, "Reduction of power losses in the tape-wound FeNiCuNbSiB nanocrystalline cores using interlaminar insulation," *IEEE Trans. Magn.*, vol. 50, no. 4, Apr. 2014, Art. no. 6300704.

[2] M. R. Islam, Y. Guo, Z. W. Lin, and J. Zhu, "An amorphous alloy core medium frequency magnetic-link for medium voltage photovoltaic inverters," *J. Appl. Phys.*, vol. 115, 2014, Art. no. 17E710.

[3] Y. Zhang, P. Sharma, and A. Makino, "Fe-Rich Fe-Si-B-P-Cu powder cores for high-frequency power electronic applications," *IEEE Trans. Magn.*, vol. 50, no. 11, Nov. 2014, Art. no. 2006804.

[4] F. Neveu, B. Allard, C. Martin, P. Bevilacqua, and F. Voiron, "A 100 MHz 91.5% peak efficiency integrated buck converter with a Three-MOSFET cascode bridge," *IEEE Trans. Power Electron.*, vol. 31, no. 6, pp. 3985–3988, Jun. 2016.
[5] J. Choi, D. Tsukiyama, Y. Tsuruda, and J. M. R. Davila, "High-frequency, high-power resonant inverter with eGaN FET for wireless power transfer," *IEEE Trans. Power Electron.*, vol. 33, no. 3, pp. 1890–1896, Mar. 2018.
[6] N. Soltau, D. Eggers, K. Hameyer, and R. W. De Doncker, "Iron losses in a medium-frequency transformer operated in a high-power DC-DC converter," *IEEE Trans. Magn.*, vol. 50, no. 2, Feb. 2014, Art. no. 7023604.
[7] P. Huang *et al.*, "Optimal design and implementation of high-voltage high-power silicon steel core medium-freqnency transformer," *IEEE Trans. Ind. Electron.*, vol. 64, no. 6, pp. 4391–4401, Jun. 2017.
[8] N. Fernando, G. Vakil, P. Arumugam, E. Amankwah, C. Gerada, and S. Bozhko, "Impact of soft magnetic material on design of high-speed permanent-magnet machines," *IEEE Trans. Ind. Electron.*, vol. 64, no. 3, pp. 2415–2413, Mar. 2017.
[9] O. de la Barrière, C. Ragusa, C. Appino, and F. Fiorillo, "Prediction of energy losses in soft magnetic materials under arbitrary induction waveforms and DC bias," *IEEE Trans. Ind. Electron.*, vol. 64, no. 3, pp. 2522–2529, Mar. 2017.
[10] E. L. Barrios, A. Ursúa, L. Marroyo, and P. Sanchis, "Analytical design methodology for litz-wired high-frequency power transformers," *IEEE Trans. Ind. Electron.*, vol. 62, no. 4, pp. 2103–2113, Apr. 2015.
[11] Z. Zhang, K. D. T. Ngo, and J. L. Nilles, "Design of inductors with significant AC Flux," *IEEE Trans. Power Electron.*, vol. 32, no. 1, pp. 529–539, Jan. 2017.
[12] S. Barg, K. Ammous, H. Mejbri, and A. Ammous, "An improved empirical formulation for magnetic core loss estimation under nonsinusoidal induction," *IEEE Trans. Power Electron*, vol. 32, no. 3, pp. 2146–2154, Mar. 2017.
[13] M. J. Jacoboski, A. D. B. Lange, and M. L. Heldwein, "Closed-form solution for core loss calculation in single-phase bridgeless PFC rectifiers based on the iGSE method," *IEEE Trans. Power. Electron.*, vol. 33, no. 6, pp. 4599–4604, Jun. 2018.
[14] C. Feeney, N. Wang, S. Kulkarni, Z. Pavlović, C. Ó. Mathúna, and M. Duffy, "Loss modeling of coupled stripline microinductors in power supply on chip applications," *IEEE Trans. Power Electron.*, vol. 31, no. 5, pp. 3754–3762, May 2016.
[15] G. Grandi, M. K. Kazimierczuk, A. Massarini, U. Reggiani, and G. Sancineto, "Model of laminated iron-core inductors for high frequencies," *IEEE Trans. Magn.*, vol. 40, no. 4, pp. 1839–1845, Jul. 2004.
[16] W. A. Roshen, "A practical, accurate and very general core loss model for nonsinusoidal waveforms," *IEEE Trans. Power Electron.*, vol. 22, no. 1, pp. 30–40, Jan. 2007.
[17] T. Hatakeyama and K. Onda, "Core loss estimation of various materials magnetized with the symmetrical/asymmetrical rectangular voltage," *IEEE Trans. Power Electron.*, vol. 29, no. 12, pp. 6628–6635, Dec. 2014.
[18] A. Hilal, M.-A. Raulet, C. Martin, and F. Sixdenier, "Power loss prediction and precise modeling of magnetic powder components in DC-DC power converter application," *IEEE Trans. Power Electron.*, vol. 30, no. 4, pp. 2232–2238, Apr. 2015.
[19] M. Owzareck, "Calculation method for core losses of electrical steel inductors in power electronic applications," in *Proc. Int. Exhib. Conf. Power Electron., Intell. Motion, Renewable Energy Energy Manage.*, Nürnberg, Germany, May 2015, pp. 1845–1852.
[20] A. Abramovitz and S. Ben-Yaakov, "RGSE-based SPICE model of ferrite core losses," *IEEE Trans. Power Electron.*, vol. 33, no. 4, pp. 2825–2831, Apr. 2018.
[21] L. A. R. Tria, D. Zhang, and J. E. Fletcher, "Implementation of a nonlinear planar magnetics model," *IEEE Trans. Power Electron.*, vol. 31, no. 9, pp. 6534–6542, Sep. 2016.
[22] A. Ruderman, B. Reznikov, and S. Busquets-Monge, "Asymptotic time-domain evaluation of a multilevel multiphase PWM converter voltage quality," *IEEE Trans. Ind. Electron.*, vol. 60, no. 5, pp. 1999–2009, May 2013.
[23] L. Dupré, O. Bottauscio, M. Chiampi, M. Repetto, and J. A. A. Melkebeek, "Modeling of electromagnetic phenomena in soft magnetic materials under unidirectional time-periodic flux excitations," *IEEE Trans. Magn.*, vol. 35, no. 5, Sep. 1999, Art. no. 41714184.
[24] J. Gyselinck, R. V. Sabariego, and P. Dular, "A nonlinear time-domain homogenization technique for laminated iron cores in three-dimensional finite-element models," *IEEE Trans. Magn.*, vol. 42, no. 4, pp. 763–766, Apr. 2006.
[25] P. Rasilo, E. Dlala, K. Fonteyn, J. Pippuri, A. Belahcen, and A. Arkkio, "Model of laminated ferromagnetic cores for loss prediction in electrical machines," *IET Electr. Power Appl.*, vol. 5, no. 5, pp. 580–588, Aug. 2011.
[26] E. Dlala, O. Bottauscio, M. Chiampi, M. Zucca, A. Belahcen, and A. Arkkio, "Numerical investigation of the effects of loading and slot harmonics on the core losses of induction machines," *IEEE Trans. Magn.*, vol. 48, no. 2, pp. 1063–1066, Feb. 2012.
[27] P. Rasilo A. Salem, A. Abdallh, F. De Belie, L. Dupré, and J. Melkebeek, "Effect of multilevel inverter supply on core losses in magnetic materials and electrical machines," *IEEE Trans. Energy Convers.*, vol. 30, no. 2, pp. 736–744, June. 2015.
[28] S. E. Zirka, Y. I. Moroz, R. G. Harrison, and N. Chiesa, "Inverse hysteresis models for transient simulation," *IEEE Trans. Power Deliv.*, vol. 29, no. 2, pp. 552–559, Apr. 2014.
[29] S. E. Zirka, Y. I. Moroz, N. Chiesa, R. G. Harrison, and H. K. Høidalen, "Implementation of inverse hysteresis model Into EMTP – Part I: Static model," *IEEE Trans. Power Deliv.*, vol. 30, no. 5, pp. 2224–2232, Oct. 2015.
[30] S. E. Zirka, Y. I. Moroz, N. Chiesa, R. G. Harrison, and H. K. Høidalen, "Implementation of inverse hysteresis model into EMTP – Part II: Dynamic model," *IEEE Trans. Power Deliv.*, vol. 30, no. 5, pp. 2233–2241, Oct. 2015.
[31] S. Jazebi *et al.*, "Duality derived transformer models for low-frequency electromagnetic transients – Part I: Topological models," *IEEE Trans. Power Deliv.*, vol. 31, no. 5, pp. 2410–2419, Oct. 2016.
[32] S. Jazebi *et al.*, "Duality derived transformer models for low-frequency electromagnetic transients – Part II: Complementary modeling guidelines," *IEEE Trans. Power Deliv.*, vol. 31, no. 5, pp. 2410–2419, Oct. 2016.
[33] S. E. Zirka, Y. I. Moroz, H. K. Høidalen, A. Lotfi, N. Chiesa, and C. M. Arturi, "Practical experience in using an topological model of a core-type three-phase transformer – no-load and inrush conditions," *IEEE Trans. Power Deliv.*, vol. 32, no. 4, pp. 2081–2090, Aug. 2017.
[34] L. A. Righi, N. Sadowski, R. Carlson, J. P. A. Bastos, and N. J. Batistela, "A new approach for iron losses calculation in voltage fed time stepping finite elements," *IEEE Trans. Magn.*, vol. 37, no. 5, pp. 3353–3356, Sep. 2001.
[35] W. Martinez, S. Odawara, and K. Fujisaki, "Iron loss characteristics evaluation using a high-frequency GaN inverter excitation," *IEEE Trans. Magn.*, vol. 53, no. 11, Nov. 2017, Art. no. 1000607.
[36] N. Steel and S. Metal, "Non-oriented electrical steel sheets," 2015. [Online]. Available: https://www.nssmc.com/product/catalog_download/pdf/D005je.pdf
[37] J. Lammeraner and M. Štafl, in *Eddy Currents*. Prague, Czech Republic: Iliffe Books Ltd., 1966, pp. 30–37.
[38] A. Ruderman and R. Welch, "Electrical machine PWM loss evaluation basics," in *Proc. Energy Efficiency Motor Driven Syst.*, Heidelberg, Germany, vol. 1, Sep. 2005, pp. 58–68.
[39] D. B. Rathnayake and S. G. Abeyratne, "Effect of semiconductor devices' output parasitic capacitance on zero-current clamping phenomenon in PWM-VSI drives," in *Proc. IEEE 10th Int. Conf. Ind. Inform. Syst.*, Sri Lanka, Dec. 2015, pp. 446–451.
[40] T. Tanaka, S. Koga, R. Kogi, S. Odawara, and K. Fujisaki, "High-carrier-frequency iron-loss characteristics excited by GaN FET single-phase PWM inverter," (in Japanese), *IEEJ Trans. Ind. Appl.*, vol. 136, no. 2, pp. 110–117, 2016.

Paavo Rasilo (M'18) received the M.Sc. (Tech.) and D.Sc. (Tech.) degrees from the Helsinki University of Technology (currently Aalto University) and Aalto University, Espoo, Finland, in 2008 and 2012, respectively.

He is currently an Assistant Professor with the Laboratory of Electrical Energy Engineering, Tampere University of Technology, Tampere, Finland. His research interests include numerical modeling of electrical machines as well as power losses and magnetomechanical effects in soft magnetic materials.

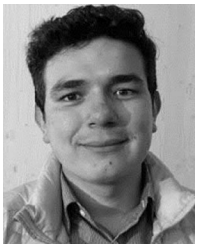

Wilmar Martinez (S'09–M'16) received the B.S. degree in electronics engineering and the M.Sc. degree in electrical engineering from Universidad Nacional de Colombia, Bogota, Colombia, in 2011 and 2013, respectively, and the Ph.D. degree in electronic function and system engineering from Shimane University, Matsue, Japan, in 2016.

He was a Postdoctoral Researcher with the Toyota Technological Institute, Nagoya, Japan, and with Aalto University, Espoo, Finland, in 2016 and 2017, respectively. He is currently an Assistant Professor with KU Leuven, Leuven, Belgium. His research interests include multiobjective optimization of power converters, evaluation of iron losses at high carrier frequency in electric motors, and high power density converters for electric vehicles, renewable energies, and smart grids.

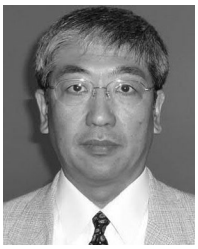

Keisuke Fujisaki (S'82–M'83–SM'02) received the B.Eng., M.Eng., and Dr.Eng. degrees in electrical engineering from the Faculty of Engineering, The University of Tokyo, Tokyo, Japan, in 1981, 1983, and 1986, respectively.

From 1986 to 1991, he conducted research on electromagnetic force applications to steel-making plants at the Ohita Works, Nippon Steel Corporation, Futtsu, Japan. From 1991 to 2010, he was a Chief Researcher with the Technical Development Bureau, Nippon Steel Corporation. From 2002 to 2003, he was a Visiting Professor with Ohita University, Oita, Japan. From 2003 to 2009, he was a Visiting Professor with Tohoku University, Sendai, Japan. Since 2010, he was a Professor with Toyota Technological Institute. His research interests include highly efficient motor drive system, magnetic multiscale, electromagnetic multiphysics, electrical motor, and power electronics.

Dr. Fujisaki received the Outstanding Prize Paper Award at the Metal Industry Committee sessions of the 2002 IEEE Industry Applications Society Annual Meeting.

Jorma Kyyrä (M'1994) received the M.Sc., Lic.Sc., and D.Sc. degrees from the Helsinki University of Technology (TKK), Helsinki, Finland, in 1987, 1991, and 1995, respectively.

Since 1985, he has been with the university in various positions. Since 1996, he has been an Associate Professor of power electronics, and since 1998, a Professor of power electronics. From 2008 to 2009, he has been the Dean with the Faculty of Electronics, Communications and Automation, TKK, and from 2009 to 2011, the Vice President of Aalto University, Espoo, Finland. He is currently the Head of the Department of Electrical Engineering and Automation with Aalto University. His research interest is power electronics at large. The power electronics group at Aalto University has expertise, e.g., in power electronics for ac drives, dc–dc converters, modeling of converters, filtering of EMI, power factor correction, and distributed power systems.

Alex Ruderman (M'07–SM'17) received the M.Sc. (Hons.) degree in electrical engineering from Leningrad Electrical Engineering Institute, Leningrad, Russia, in 1980, and the Ph.D. degree in electromechanical engineering from Leningrad Polytechnic Institute, Leningrad, Russia, in 1987.

From 1995 to 2003, he was a Research Scientist with Intel Microprocessor Development Center, Haifa, Israel, investigating microprocessor thermal stabilization, power delivery, fast and accurate static timing calculation including coupling, and other issues. After teaching several electronics-related courses, from 2004 to 2005, at Bar Ilan University, Ramat Gan, Israel, and the Holon Institute of Technology, Holon, Israel, as an Adjunct Faculty, he joined Elmo Motion Control, Petach Tikva, Israel, the makers of compact intelligent servo drives, as a Chief Scientist. Since 2013, he has been an Associate Professor with the Department of Electrical and Computer Engineering, School of Engineering, Nazarbayev University, Astana, Kazakhstan, and the Head of Power Electronics Research Laboratory. His research interests include multilevel converters voltage/current quality and natural balancing mechanisms. He has coauthored more than 40 conference and journal papers on the subjects.